IEEE NSS-MIC, Seoul, South Korea, 2013, M18-26

Calculated attenuation correction for awake small animal brain PET studies

Georgios Angelis, Matthew Bickell, Andre Kyme, William Ryder, Lin Zhou, Johan Nuyts, Steven Meikle and Roger Fulton

***Abstract*—Attenuation correction of small animal PET data is very important when quantitative images are of interest. Attenuation correction coefficients are conventionally obtained via a transmission or a computed tomography scan, which require anaesthetisation of the animal. However, in the context of awake and/or freely moving animals, where animal motion is compensated via appropriate motion tracking and correction techniques, anaesthetisation is no longer required. In this work we investigate the accuracy of a transmission-less attenuation correction approach based on the segmentation of the motion corrected emission image. Results on both phantom and real rat data acquired on the microPET Focus220 scanner, indicate good agreement between the segmentation based and conventional transmission based approach ($\sim$ 2% difference). In addition, the segmentation based approach has the potential to eliminate noise propagation from the measured transmission data to the reconstructed attenuation corrected emission images.**

I. Introduction

IMAGING awake and/or freely moving small animals with positron emission tomography (PET) is a promising approach towards a better understanding of neurochemical and physiological processes *in vivo* [1, 2]. The advantage of such an approach is that it eliminates the impact of anaesthetic drugs on the biochemistry of the animal's brain, while also making it possible to monitor the biological and physiological response of the brain to external stimuli [3].

Previous studies have demonstrated the importance of attenuation correction (AC) on the quantitative accuracy of the reconstructed images for both rats and mice in emission tomography [4, 5]. Conventionally, AC is performed using either a transmission (TX) or a computed tomography scan. Although, both approaches are considered highly accurate, they require the immobilisation of the animal, often using anaesthesia. Since anaesthesia can be avoided during the emission scan by employing sophisticated motion tracking and correction approaches [1], it would be preferable to avoid it for the transmission scan as well.

Several techniques have been proposed in order to calculate the attenuation correction factors without the need of a transmission scan. Recently proposed techniques involve the exploitation of consistency conditions between the attenuation and emission data [6], as well as the joint estimation of the activity concentration and the attenuation coefficients via an iterative scheme [7]. Although, these approaches appear to be very promising, the coupling between the emission and attenuation distributions results in a non-concave objective function, which is more susceptible to local-maxima. A different approach involves the generation of a convex hull of the object based on the segmentation of the emission sinograms or reconstructed images and assuming uniform attenuation coefficients [8, 9, 13].

In the context of awake and/or freely moving animals the latter approach is very attractive since it leads to noiseless attenuation maps and eliminates the need to co-register the transmission and emission data. Although the convex hull of the object could be created by segmenting the motion corrected emission sinogram as in [7, 13], it may lead to misregistering parts of the object to the background due to incorrect weighting for lost events due to motion.

Therefore, the objectives of this work are to develop and evaluate a method for calculating the AC factors without anesthetizing the animal or performing a transmission scan. The convex hull of the animal's head is generated based on the segmentation of the reconstructed motion corrected emission images, while attenuation coefficients for soft tissue are assumed for the entire head [8, 9]. The efficiency and accuracy of the segmentation-based AC approach was assessed against a TX-based approach using measured phantom data, as well as data from anaesthetised and awake tube-bound rats.

II. Methods

A. Image Segmentation

The goal of the segmentation algorithm is to successfully differentiate the object (i.e. rat's head) from the background. In this work, we used an automated histogram-based thresholding approach [10], which calculates the optimal threshold by maximising the variance between the distribution of the object and the distribution of the background.

B. Phantom Data

The quantitative accuracy of the segmentation-based method was evaluated by means of a phantom scan. The phantom consisted of two cylindrical compartments (12 mm inner diameter) embedded in a warm background (42 mm inner diameter). The phantom was filled with $\sim$38 MBq of fluorine-18 with a contrast ratio of 3:1 between the warm background and one cylindrical insert (i.e. hot), while the other cylindrical insert was filled with inactive water (i.e. cold). A robotic arm was used to suspend the phantom in the centre of the field of view of the microPET Focus 220 scanner (Preclinical Solutions, Siemens Healthcare Molecular Imaging, USA) in order to avoid the attenuation

G. Angelis, A. Kyme, W. Ryder, R. Fulton and S. Meikle are with the Brain & Mind Research Institute and the Faculty of Health Sciences, The University of Sydney, Sydney, NSW 2050, Australia.

M. Bickell, L. Zhou, J. Nuyts are with the Nuclear Medicine and Medical Imaging Research Center, KU Leuven, Belgium.

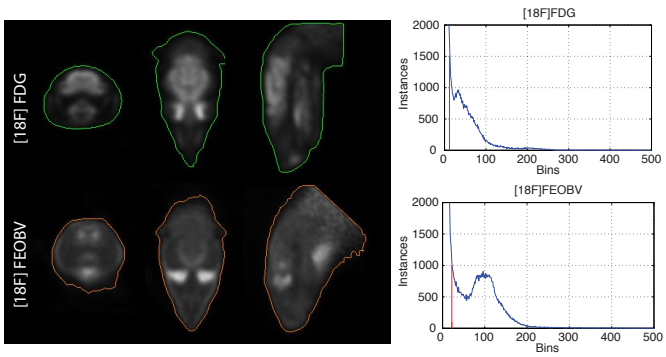

Fig. 1. Demonstration of the thresholding algorithm (coloured outlines) on two awake rat studies with diverse activity distribution: (top) [18F]FDG and (bottom) [18F]FEOBV. On the right hand side are histograms for the two rat studies, as well as the threshold value (red line).

effects of the bed and it was scanned for one hour collecting approximately 270 million events.

In order to emulate an almost noiseless TX-based attenuation map, a very long TX scan, equivalent to 32 passes of a Co-57 point source (57 MBq), was acquired. One pass is defined as a complete (spiral) excursion of the point source through the scanner and back (approximately 8 minutes). Fewer passes imply fewer recorded events and therefore noisier reconstructed attenuation maps. The TX listmode data were then split into smaller datasets corresponding to more realistic TX acquisitions of 1, 2 and 4 passes, representing different noise levels. The transmission data were then histogrammed using single slice rebinning (SSRB) and reconstructed using a maximum likelihood transmission reconstruction [11]. Since the phantom is made of thick perspex walls ($\sim$4 mm) that are non-radioactive, segmentation of the reconstructed emission image would lead to severe underestimation of the true object size and consequently underestimating the attenuation correction factors. Therefore, only for this phantom experiment, the convex hull of the object was extracted from the segmentation of the attenuation map using the TX data acquired with 4 passes (which represents a realistic case).

C. Awake Rat Data

In addition to the phantom data, the segmentation-based AC approach was also applied to real rat data acquired on the microPET Focus220 scanner. A rat was injected with 60 MBq of [^{18}F]FDG and scanned for 10 minutes, collecting approximately 100 million events. In order to verify the approach against a TX-based AC approach the rat was later anaesthetised and scanned for a further 20 minutes, collecting approximately 70 million events. After the emission scan and while the rat was still under anaesthesia, a TX scan equivalent to 4 passes of a point source was acquired. Finally, the two emission scans were co-registered in order to assist a quantitative comparison. All reconstructions were performed using an event-by-event motion compensating list-mode maximum likelihood expectation maximisation (LM-MLEM) algorithm [12] (20 iterations, 10 subsets). No corrections for scatter or random events were applied to the acquired data, assuming that they were negligible.

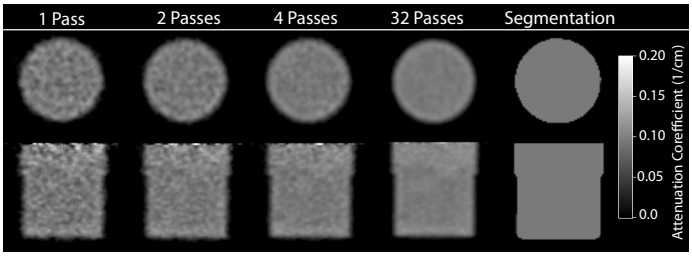

Fig. 2. Transverse (top) and sagittal (bottom) slices for the reconstructed attenuation maps using 1, 2, 4 and 32 passes, compared against the segmented map. One pass is defined as a complete (spiral) excursion of the point source through the scanner and back. Fewer passes imply fewer recorded events and therefore noisier reconstructed attenuation maps.

III. Results and Discussion

A. Image Segmentation

The efficiency of the automated image segmentation algorithm was assessed on two examples of awake tube-bound rat acquisitions, with relatively diverse activity distributions: an [^{18}F]FDG acquisition with a relative high uptake in the brain and less in the rest of the head (including skin and skull) and a [^{18}F]FEOBV scan with a relatively more uniform uptake throughout the rat's head (Fig. 1). In both cases the segmentation algorithm managed to differentiate the head from the backgound, even though for the [^{18}F]FDG acqusition the tracer uptake in the skin was very low.

B. Phantom Data

The reconstructed attenuation maps, which were used for TX based AC are shown in Fig. 2. Each map represents different acquisition times and therefore different noise levels, which can potentially propagate in the reconstructed image. In terms of image quality, even the least number of passes, did not generate a very noisy image, mainly because the source was relatively strong and the data were histogrammed using SSRB. Fig. 3a shows the image roughness^{footnotemark} versus the mean value in the reconstructed attenuation maps as a function of region size (5 circular regions ranging from 1 to 5 mm radius) in an attempt to quantify the noise level in the reconstructed attenuation maps. In this work, the segmented attenuation map was assigned with the attenuation coefficient for water and soft tissue (0.096 cm^{-1}). A profile through the centre of the transverse reconstructed attenuation maps is shown in Fig. 3b, with the one-pass image being noticably noisier than the rest.

The reconstructed emission images of the compartment phantom, using different attenuation maps for AC, are shown in Fig. 4. Although, the reconstructed attenuation maps had different noise properties, the reconstructed emission images appear to be very similar. The noise characteristics of the AC reconstructed emission images, using different attenuation maps are shown in Fig. 5. The image roughness versus the percentage bias is plotted as a function of iterations for the hot cylinder (a) and a region of the same size in the warm background (b). In both regions bias did not vary more than 1% between different

[0]Image roughness is defined as the coefficient of variation of the pixels within a region and represents the pixel-to-pixel variability within that region.

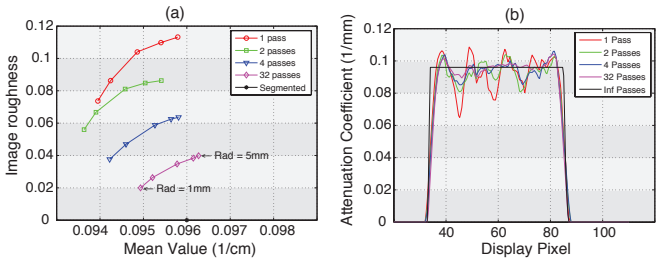

Fig. 3. (a) Regional mean vs. image roughness for 5 circular regions within the reconstructed attenuation maps (1 to 5 mm radius). (b) Line profiles through the centre of the transverse slice of the attenuation maps shown in Fig. 2.

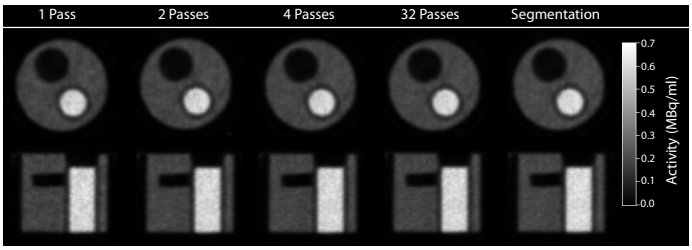

Fig. 4. Transverse (top) and sagittal (bottom) slices for the reconstructed emission images of the compartment phantom using different attenuation maps to perform AC. All reconstructions used 14 iterations (10 subsets).

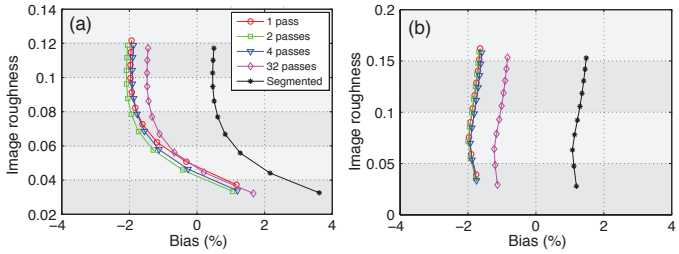

Fig. 5. Image roughness versus the percentage bias as a function of iterations for the hot cylinder (a) and an equivalent sized region in the warm background (b) of the attenuation corrected images using different methods. In both regions bias did not vary more than 1% between different TX based approaches, while the relative bias between TX and segmentation based AC was approximately 2%. In all curves, iterations are increasing from bottom to top.

TX-based approaches, while the relative bias between TX and segmentation-based AC correction was approximately 2%. In addition, it appears that the use of the segmented attenuation map leads to overestimation of the activity in both regions. This could be attributed to the fact that the segmented map is usually one or two pixels wider than the measured attenuation map and the selected attenuation coefficient was higher than the value estimated by the measured data (Fig. 3). In terms of noise, there is a small increase in variance when more noisy attenuation maps were used (i.e. fewer passes). However, the high-statistics TX based approach demonstrates very similar noise levels compared to the segmented image. Finally, the line profiles on the transverse reconstructed emission images along (a) the centers of the hot and the cold inserts, and (b) the uniform region between the two inserts are shown in Fig. 6.

C. Awake Rat Data

Fig. 7 shows orthogonal slices of the anaesthetised rat study, which correspond to the reconstructed non AC emission image

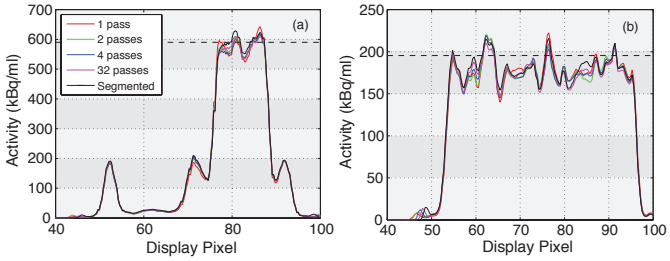

Fig. 6. Line profiles on the transverse reconstructed emission images along (a) the centers of the hot and the cold inserts, and (b) the uniform region between the two inserts. The horizontal dashed line corresponds to the true activity as measured in the dose calibrator. All reconstruction approaches showed very similar behavior, yet the reconstruction with the 1-pass attenuation map appeared to be slightly noisier.

(bottom) and the TX based attenuation map (top). The yellow outline represents the threshold used to segmented the emission image and is overlayed with the actual reconstructed TX-based attenuation map. The segmented image appears to be a couple of voxels wider than the measured TX based attenuation map, which could potentially lead to overestimation of the activity in the AC reconstructed image. However, this could potentially compensate for the fact that the segmented image assumes uniform attenuation factors and does not account for the higher attenuation caused by the skull.

Fig. 8 shows transverse (top) and coronal (bottom) slices of the reconstructed emission images for the anaesthetised (a-c) and the awake tube-bound (d) rat studies (corrected for isotope decay to match the activity of the awake scan). Different attenuation maps were used to reconstruct each image: (a) no AC, (b) the measured TX-based attenuation map and (c) the segmented emission image. The awake rat segmented AC image (d) is also shown, after motion correction. Similar to the phantom data, images reconstructed with the TX-based and the segmention-based approaches appear to be qualitatively very similar, both in terms of noise and intensity. A more quantitative comparison can be achieved by plotting a line profile through the striatum of the coronal images (Fig. 9 - red line). Good agreement is observed between the TX-based and the segmentation-based AC approaches for the anaesthetised rat acquisition (Fig. 9I), as well as between the TX-based AC anaesthetised rat and the segmentation-based awake tube-bound rat (Fig. 9II).

IV. Conclusions

In this work we evaluated the accuracy of a segmentation based AC approach, using real phantom and rat data for awake animal PET studies. The quantitative accuracy of the segmentation based AC approach is comparable to a TX based approach ($\sim$2% difference), while it has the potential to avoid propagation of noise from the TX data to the emission image. Future work will involve comparison against a 3D TX reconstruction approach, where improvements in resolution could be expected at the expense of more noise in the TX data. In addition, application to a wide range of diverse radiotracer distributions is imperative to assess the effectiveness of the segmentation.

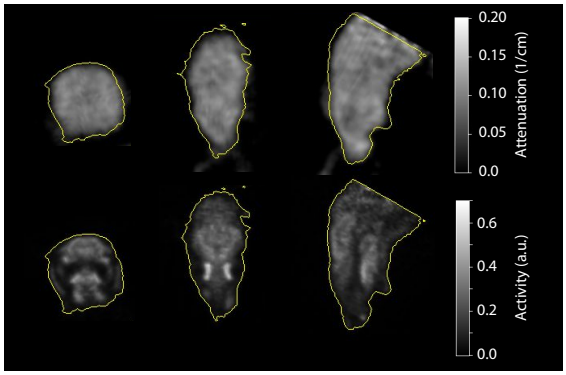

Fig. 7. Orthogonal slices of the reconstructed attenuation (top) and emission (bottom) images of anesthetized rat study. The image-based segmented attenuation map was created by thresholding the emission image using Otsu's segmentation (yellow outline). The segmented image appears to be one or two voxels wider than the measured TX based attenuation map, which could potentially lead to overestimation of the activity in the AC reconstructed image.

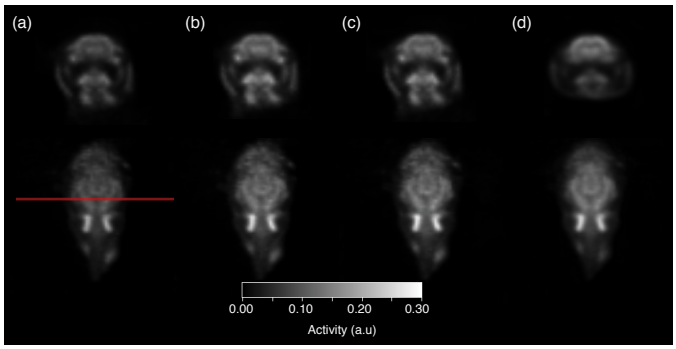

Fig. 8. Transverse (top) and coronal (bottom) slices of AC emission images for the anesthetized rat (corrected for decay): (a) no AC, (b) TX based, (c) segmentation based. The AC image, using the segmented images approach, of the awake rat after motion correction is shown in (d).

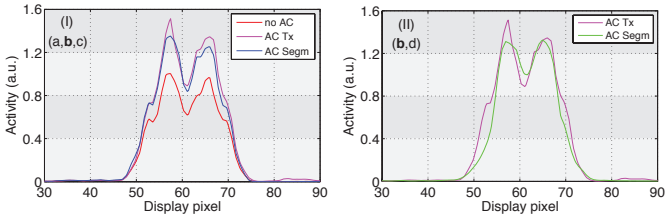

Fig. 9. Profiles through the striata (red line) comparing different AC approaches for the anesthetized rat (left), and comparing the AC awake rat against the TX based AC anesthetized rat (right). The profiles through the striatum indicate good agreement between the TX based and the segmentation based AC approaches.

REFERENCES

[1] A. Z. Kyme, V. W. Zhou, S. R. Meikle, C. Baldock, R. R. Fulton, "Optimised Motion Tracking for Positron Emission Tomography Studies of Brain Function in Awake Rats", *PLoS ONE*, **6**(7), e21727, 2011

[2] D. Schulz, S. Southekal, S. S. Junnarkar, J.-F. Pratte, M. L. Purschke, S. P. Stoll, B. Ravindranath, S. H. Maramraju, S. Krishnamoorthy, F. A. Henn, P. O'Connor, C. L. Woody, D. J. Schlyer, P. Vaska, "Simultaneous assessment of rodent behavior and neurochemistry using a miniature positron emission tomograph", *Nature Methods* **8**, 347352, 2010

[3] G. Hart, G. I. Angelis, A. Kyme, W. J. Ryder, S. R. Meikle, A. Parmar, R. R. Fulton, B. Balleine, "MicroPET Assessment of Regional Brain Activation During Pavlovian Learning in Conscious Unrestrained Rats", *WMIC Meeting 2013*, 2013

[4] P. L. Chow, F. R. Rannou, A. F. Chatziioannou, "Attenuation correction for small animal PET tomographs", *Phys. Med. Biol.* **50**(8), 1837-1850, 2005

[5] D. Hwang and G. L. Zeng GL "A new simple iterative reconstruction algorithm for SPECT transmission measurement". *Med. Phys.* **32**(9), 2799–804, 2005

[6] A. Welch, R. Clack, F. Natterer, G. T. Gullberg, "Toward accurate attenuation correction in SPECT without transmission measurements", *IEEE Trans. Nucl. Sci.* 16(5), 532, 1997

[7] J. Nuyts, P. Dupont, S. Stroobants, R. Benninck, L. Mortelmans, P. Suetens, "Simultaneous maximum a posteriori reconstruction of attenuation and activity distributions from emission sinograms", *IEEE Trans. Med. Imag.* 18(5), 393–403, 1999

[8] M. Bergström, J. Litton, L. Eriksson, C. Bohm, G. Blomqvist, "Determination of object contour from projections for attenuation correction in cranial positron emission in tomography", *IEEE Trans. Nucl. Sci. 27*, 549–554, 1982

[9] S. Siegel and M. Dahlbom, "Implementation and evaluation of a calculated attenuation correction for PET", *IEEE Trans. Nucl. Sci. 39*, 1117–1121, 1992

[10] N. Otsu, "Threshold selection method from gray-level histograms", *IEEE Trans. Sys. Man Cyber.* **9**(1), 62–66, 1979

[11] J. Nuyts, P. Dupont, S. Stroobants, A. Maes, L. Mortelmans, P. Suetens, "Evaluation of maximum-likelihood based attenuation correction in positron emission tomography", *IEEE Trans. Nucl. Sci.*, **46**(4), 1136–1141, 1999

[12] A. Rahmim, K. Dinelle, J. C. Cheng, M. A. Shilov, W. P. Segars, S. C. Lidstone, S. Blinder, O. G. Rousset, H. Vajihollahi, B. M. W. Tsui, D. F. Wong and V. Sossi, "Accurate event-driven motion compensation in high-resolution PET incorporating scattered and random events", *IEEE Trans. Med. Imaging*, **27**(8), 1018–1033, 2008

[13] C. Michel, A. Bol, A. G. De Volder, A.M Gofnet, "Online brain attenuation correction in PET: towards a fully automated data handling in a clinical environment." *Eur. J. Nucl. Med.*, **15**, pp. 712–718, 1989